Bayesian Estimation of Non-Rigid Mechanical Parameters Using Temporal Sequences of Deformation Samples

Shan Yang and Ming C. Lin[1]

Abstract— **Material property has great importance in medical robotics. The mechanical properties of the human soft tissue, are important to characterize the tissue deformation of each patient. The (recovered) elasticity parameters can assist surgeons to perform better pre-op surgical planning and enable medical robots to carry out personalized surgical procedures. In this paper, we present a novel algorithm on mechanical-property estimation from a temporal sequence of deformation samples. It does not require an external force-application measurement device or landmark-based displacement tracking. We test our approach on the reconstruction the Young's modulus of a human heart and further validate the results derived from videos using known parameters of tennis and foam balls.**

I. INTRODUCTION

Non-rigid materials are widely used in medical robotics, design and manufacturing, virtual surgery for soft robot planning, procedural rehearsal and training, etc. Identification of mechanical properties, such as tissue elasticity parameters, is critical to enable medical robots to safely operate within highly unstructured, deformable human bodies and to compute desired, accurate force feedback for individualized haptic display characterized by patient-specific parameters. In addition to medical robots, simulations are also increasingly used for rapid prototyping of clinical devices, pre-operation planning of medical procedures, virtual training exercises for surgeons and supporting personnel, etc. And, bio-tissue elasticity properties are central to developing realistic and predictive simulation and for designing responsive, dexterous surgical manipulators. Furthermore, with increasing interest in 3D printing for rapid creation of soft robots consisting of flexible materials, the ability to easily acquire material properties from existing sensor data, such as medical images and videos, can help to replicate similar material properties.

Traditional stress-strain matching methods have been practiced for decades to measure the mechanical properties of deformable bodies [1]. Special external force measuring devices are often applied. Landmarks on the deformable bodies are usually used in these methods for measuring displacement fields. Following the wide adoption of ultrasound, elastography[2] emerged, which estimates relative elasticity properties by measuring both the deformation of the tissue via ultrasound images and explicitly measuring the external force using special devices. In the last decade or so, numerical methods, such as inverse Finite Element Methods (FEM) [3], [4], were proposed to estimate mechanical properties of deformable body without the measurement

of the displacement field. But, these techniques are generally limited to quasi-static deformation process. Human tissues, such as the heart, are often in a dynamic state.

In this paper, we propose a novel Bayesian elasticity-parameter estimation algorithm for deformable bodies using temporal sequences of deformation samples. These deformation samples may be medical images, such as those from ultrasound and echocardialgram, videos, or hand sketches. The samples reflect the 4-dimensional (or 3D) behavior of the deformable bodies by providing a temporal sequence of 3D (or 2D) shapes in motion. Our method follows the iterative optimization from the Lavenberg-Marquardt Algorithm [5], [6]. But, we address the problem using the Bayesian framework. Given the temporal sequences input, we adopt a probabilistic graphical model [7], [8], the unscented Kalman Filter [9], to continuously refine the estimated elasticity parameters by matching the simulated deformation (generated by FEM simulation) to the input temporal sequences of (captured) deformation samples. The geometric models of the deformable bodies are reconstructed from the given measurements, e.g. videos.

In contrast to the traditional strain-stress matching methods [10], [11], [12], [13], elastography methods [14], [15], [16], and the more recent inverse FEM [3], [4], we are able to recover the mechanical parameters of the deformable bodies by tracking and matching a temporal sequence of deformation samples with simulated deformation. Similar to the inverse FEM, our approach utilizes the implicitly known or computed external force as the boundary condition. But, we further maximize the utilization of the input video by constructing the posterior probability distribution of the estimated parameters using the given temporal sequence of deformation samples. We validate the effectiveness of our framework by recovering the mechanical parameters of a tennis ball and a foam ball from videos captured by high-speed cameras.

The key results of this work include

- An alternative approach to dynamically track the surface of a deformable body in motion;
- Reconstruction of non-rigid mechanical properties from temporal sequences of deformation samples using a probabilistic, graphical model.

The rest of the paper is organized as follows. Section II provides a review of related work. We describe our Bayesian framework for elasticity parameter estimation from temporal sequences of deformation samples in Section III and present the validation experiments and results in Section IV.

[1]The authors are with the Department of Computer Science, University of North Carolina at Chapel Hill, NC 27599, USA {alexyang,lin}@cs.unc.edu

II. RELATED WORK

In this section, we highlight some research on mechanical property characterization, bio-tissue modeling, and machine learning for modeling dynamical systems.

Mechanical property characterization has received attention across different fields. Traditional mechanical property identification methods in robotics rely largely on the uniaxial stress-strain matching experiment. The uniaxial stress-strain matching experiment usually requires a device for external force measurement and a landmark based method for displacement field measurement. With the measured stress and strain, these methods find the best-fit relationship that captures the mechanical property of the object(s) of interest. Early research on mechanical property characterization of human skin, dated nearly a century ago [17]. Glaser et al. [18] standardized the uniaxial stress-strain matching method. Later on, this class of method was applied to identify the mechanical property of human organ, such as breast [19], [20] and liver [21], [22]. The major limitation of such methods is the need for explicit measurements of the stress and the strain.

Elastography algorithms [14], [15], [16] were proposed to avoid the explicit measurement of the displacement. This class of methods [23], [24], [25] compute the displacement field from the distance between two medical images. External device is still required for both the force exertion on the soft tissue and the external force measurement. Special vibrator were placed inside the organ [26] to complete the procedure. Other than distance-field-based methods for high-resolution magnetic resonance medical images, other video based method measure the displacement field from the video [27]. One limitation for this class of methods is that they require a device both to measure the external force and to exert external force on the deformable bodies.

Material design algorithms have also been proposed in Computer Graphics to recover the mechanical properties of a deformable body, given external forces and displacement fields. Bickel et al. [28] proposed to design the mechanical properties of a deformable body given external forces, displacement, and a set of base materials. Following this work, Xu et al. [29] optimized the mechanical property distribution of a deformable body with user interaction. The interaction provided the external force. This class of methods is especially useful for objects that are easy to measure the external force and the resulting displacement field. However, in many real-life situations special device needs to be designed for each designated scenario.

Inverse finite element methods use the implicitly known or computed external force to recover the mechanical property. Lee et al. proposed a model to estimate the Young's modulus based on low-resolution CT images and no external force is required to set the boundary condition [4]. The most recent work on identification of mechanical properties based on surface tracking [30] proposed a decoupled iterative tracking and parameter estimation framework. They applied a combined probabilistic physically-based method for surface tracking. Then, the tracked surfaces of the static state are the input to the parameter estimation framework. This approach does not require external force to be measured, but uses the gravity as the boundary condition. This class of methods avoid both the explicit measurement of external force and the displacement field. But the input references need to be in static state.

Probabilistic graphical models, such as Kalman Filter and Hidden Markov Model (HMM), have been used for both state estimation and parameter identification of dynamical systems. E.J. Lefferts et al. applied Kalman Filter for estimation of spacecraft attitude [31]. Kalman filters have been widely used in tracking of dynamical systems and parameter estimation, including rigid-body tracking [32], [33], motion retargeting [34], geometric contour tracking [35], and more. We adopt a tightly coupled framework using FEM-based state estimation and unscented Kalman Filter (UKF) for parameter identification.

III. METHOD

Given a temporal sequence of deformation samples, such as ultrasound videos, high-speed camera videos, etc., the goal is to recover the mechanical properties of the non-rigid body in motion. Our framework uses the unscented Kalman Filter (Sec. III-D) for the estimation of elasticity parameters and a tightly coupled module for hidden state estimation (Sec. III-E) for deformable body undergoing motion. The input to our framework are the observed temporal sequence of deformation samples and the computed boundary condition. Our framework then computes the optimized the mechanical properties and the tracked surfaces of the deformable body in motion. The overview of our framework is given in Fig. 1.

A. Generalized Dynamic Process and Decoupled State Parameter Estimation

We first give an abstract model for the general dynamic process. The discrete-time dynamic deformation process can be described by a dynamic state-space model. We will use subscript k for the kth iteration for the dynamic process and subscript n for the nth deformation sample in the sequence. The model has the hidden system state $\mathbf{x}_k$ with noise, the corresponding observation $\mathbf{y}_k$ with noise, the hidden parameter $\mathbf{w}_k$, an update function $\mathbf{f}(\mathbf{x}; \mathbf{w})$ and an observation function $\mathbf{h}(\mathbf{x}; \mathbf{w})$. The model is given as:

$$\mathbf{x}_k = \mathbf{f}(\mathbf{x}_{k-1}; \mathbf{w}) \qquad (1)$$

$$\mathbf{y}'_k = \mathbf{h}(\mathbf{x}_k; \mathbf{w}) \qquad (2)$$

$\mathbf{y}'_k$ equals to $\mathbf{y}_k$ when the hidden state and the hidden parameters are optimized.

When applied to our discrete-time dynamic deformation process, the hidden system state $\mathbf{x}$ consists of the displacement $\mathbf{u}$, the velocity $\dot{\mathbf{u}}$ and the acceleration $\ddot{\mathbf{u}}$.

$$\mathbf{x} = [\mathbf{u} \ \dot{\mathbf{u}} \ \ddot{\mathbf{u}}] \qquad (3)$$

The observation $\mathbf{y}$ is the key frame configurations which is the displacement of the key frame deformations. The update
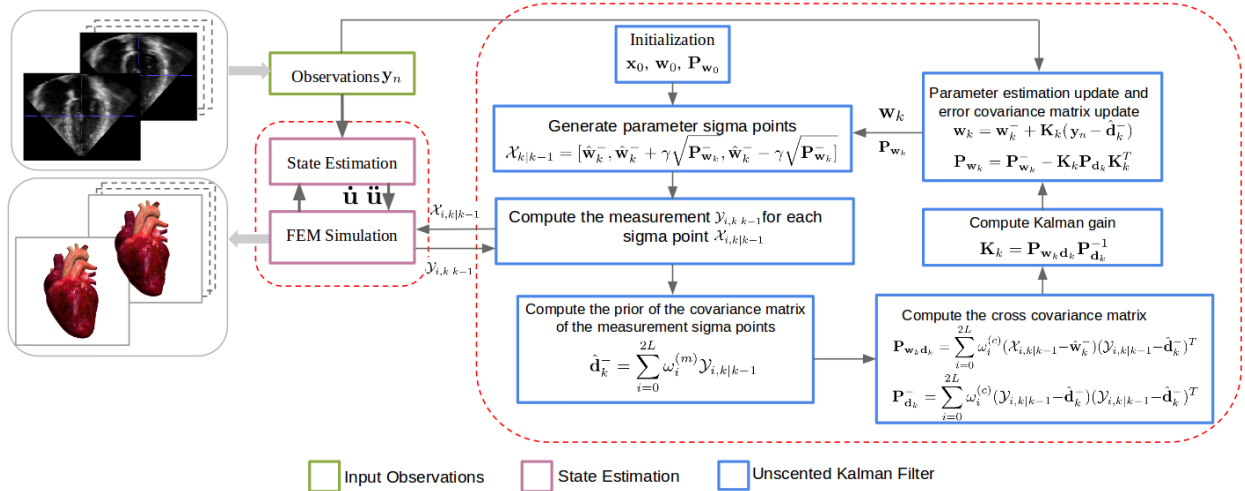
Fig. 1. **The Flow Chart of Our Framework.** Our framework takes a temporal sequence of deformation samples as the input. The UKF takes in the observations and drives the finite element simulation by optimizing both the hidden parameter and hidden states.

function $\mathbf{f}$ is the integrator. For different time discretization method, the update function $\mathbf{f}$ is different. The observation function $\mathbf{h}$ is the transformation matrix from $\mathbf{x}$ to $\mathbf{y}'$ with noise added.

Our dynamic elasticity parameters estimation problem can be stated as using the above dynamic state-space model for estimation of hidden system variables (including *states* and *parameters*) based on the keyframe observations.

B. Deformable Body Modeling

We use Finite Element Method (FEM) for the spacial integration in deformable body simulation. The governing equation for deformable bodies,

$$
\begin{aligned}
&\int_{\Omega} \delta\mathbf{u}^T \rho\ddot{\mathbf{u}} \, \mathrm{d}\Omega + \int_{\Omega} \delta(\boldsymbol{\varepsilon})^T \boldsymbol{\sigma} \, \mathrm{d}\Omega - \\
&\int_{\Omega} \delta\mathbf{u}^T \mathbf{b} \, \mathrm{d}\Omega - \int_{\Gamma} \delta\mathbf{u}^T \mathbf{t} \, \mathrm{d}\Gamma = 0,
\end{aligned}
\tag{4}
$$

with $\mathbf{u}$ as the displacement field, ρ as the mass density, $\boldsymbol{\varepsilon}$ as the strain tensor, $\boldsymbol{\sigma}$ as the stress tensor, $\mathbf{b}$ as the body force and $\mathbf{t}$ as the tractions on the boundary Γ of the deformable body Ω. We use incompressible, linear stress-strain model in this paper. For linear stress-strain model, it assumes that the relation between stress and strain can be represented by a linear function. We apply the Lamé material with the Lamé's first and second parameter computed from the Young's modulus E and the Poisson's ratio ν. Lamé material model is a widely used simple linear material model. Though the linear material model is not accurate to approximate large deformations, for our application, it is accurate enough to identify different mechanical properties of various materials. Because we assume incompressibility, we use 0.45 as the Poisson's ratio. The Young's modulus E is the parameter we will optimize using our framework. FEM combined with the Newmark implicit time integration method forms the update function Eqn. 1

C. Bayesian Parameter Estimation

For Bayesian parameter estimation, we estimate the posterior probability distribution of the parameters $\mathbf{w}_k$,

$$
p(\mathbf{w}_k|\mathbf{y}_{1:n})
\tag{5}
$$

based on the observations,

$$
\mathbf{y}_{1:n} = \mathbf{y}_1, \mathbf{y}_2, \ldots, \mathbf{y}_n
\tag{6}
$$

To motivate our reason for choosing unscented Kalman Filter as the estimation method, we will first give a brief introduction of the Recursive Bayesian Estimation algorithm. Recursive Bayesian estimation algorithm filters the posterior probability density function recursively for new observations. According to Bayes' theorem, the posterior probability density can be expressed as,

$$
p(\mathbf{w}_k|\mathbf{y}_{1:n}) = \frac{p(\mathbf{y}_n|\mathbf{w}_k)p(\mathbf{w}_k|\mathbf{y}_{1:n-1})}{p(\mathbf{y}_n|\mathbf{y}_{1:n-1})}
\tag{7}
$$

We will not give details on every term in Eqn. 7. We focus on the hidden parameter transition prior $p(\mathbf{w}_k|\mathbf{w}_{k-1})$ and the observation likelihood densities $p(\mathbf{y}_n|\mathbf{w}_k)$. The computation of the hidden parameter transition prior $p(\mathbf{w}_k|\mathbf{w}_{k-1})$ depends on the update function $\mathbf{f}(\mathbf{x}; \mathbf{w})$. In our application, the state update function $\mathbf{f}(\mathbf{x}; \mathbf{w})$ is nonlinear. Thus we need an approximation method.

The basic Kalman Filter models the densities in Eqn. 7 by Gaussian distributions. And it assumes that the state posterior probabilistic density can consistently be minimized by updating only the first (mean) and second order moments (covariance) of the true probabilistic densities. The extended Kalman Filter applies the basic Kalman Filter to nonlinear dynamic state-space system by first linearize it using Taylor series. This linearization affects the accuracy of the estimation process. The unscented Kalman Filter approaches the nonlinear problem differently. Instead of linearizing the system using Taylor series, it uses a general deterministic sampling framework, or the sigma-point approach. Thus we choose to use unscented Kalman Filter as our basic estimator for our dynamic elasticity-parameter estimation problem.

D. Unscented Kalman Filter for Parameter Estimation

The unscented Kalman Filter [9] handles the nonlinear problem with the idea that it is easier to approximate a random variable than a non-linear function. Like both basic Kalman filter and extended Kalman filter, the unscented Kalman filter consists of two steps: the prediction step and the correction step. In order to do parameter estimation, we first construct a mapping between the measured observation $\mathbf{y}'$, state $\mathbf{x}$ and the parameters $\mathbf{w}$. In the following, we will use $\mathbf{d}$ for $\mathbf{y}'$. The observation $\mathbf{y}$ equals to the measured observation $\mathbf{d}$ when the state $\mathbf{x}$ and the parameters $\mathbf{w}$ are optimized. We define a function $\mathbf{g}$ as follows,

$$\mathbf{d}_k = \mathbf{g}(\mathbf{x}_k, \mathbf{w}_k) \tag{8}$$

We will use superscript minus for prior probabilistic densities, $\mathbf{P}$ for covariance matrix, hat symbol for the mean of the random variable, subscript k for the current estimation iteration and L as the size of the parameter vector $\mathbf{w}$.

1) Initialize the mean of the parameters and the covariance matrix of the parameters

$$\hat{\mathbf{w}}_0 = E[\mathbf{w}_0] \tag{9}$$

with $\mathbf{w}_0$ as the initial guess of the parameters

$$\mathbf{P}_{\mathbf{w}_0} = E[(\mathbf{w}_0 - \hat{\mathbf{w}}_0)(\mathbf{w}_0 - \hat{\mathbf{w}}_0)^T] \tag{10}$$

2) For each estimation iteration k: Compute the prior of the mean of the parameters and the prior of the covariance of the parameters as,

$$\hat{\mathbf{w}}_k^- = \hat{\mathbf{w}}_{k-1} \tag{11}$$

$$\mathbf{P}_{\mathbf{w}_k}^- = \mathbf{P}_{\mathbf{w}_{k-1}} \tag{12}$$

Select a set of sigma points $\mathcal{X}_{k|k-1}$. The columns of the matrix $\mathcal{X}_{k|k-1}$ are the sampled parameters.

$$\mathcal{X}_{k|k-1} = [\hat{\mathbf{w}}_k^-, \hat{\mathbf{w}}_k^- + \gamma\sqrt{\mathbf{P}_{\mathbf{w}_k}^-}, \hat{\mathbf{w}}_k^- - \gamma\sqrt{\mathbf{P}_{\mathbf{w}_k}^-}] \tag{13}$$

where $\gamma = \sqrt{L + \lambda}$. The matrix expands as,

$$\begin{aligned}
\mathcal{X}_{0,k|k-1} &= \hat{\mathbf{w}}_k & i &= 0 \\
\mathcal{X}_{i,k|k-1} &= \hat{\mathbf{w}}_k + (\gamma\sqrt{\mathbf{P}_{\mathbf{w}_k}^-})_i & i &= 1, \ldots, L \\
\mathcal{X}_{i,k|k-1} &= \hat{\mathbf{w}}_k - (\gamma\sqrt{\mathbf{P}_{\mathbf{w}_k}^-})_i & i &= L+1, \ldots, 2L
\end{aligned} \tag{14}$$

The weights $\omega^{(m)}$ for computing the mean of the sigma-points and the weights $\omega^{(c)}$ for computing the covariance matrix of the sigma-points are,

$$\begin{aligned}
\omega_0^{(m)} &= \frac{\lambda}{L+\lambda} & i &= 0 \\
\omega_0^{(c)} &= \frac{\lambda}{L+\lambda} + (1 - \alpha^2 + \beta) & i &= 0 \\
\omega_i^{(m)} &= \omega_i^{(c)} = \frac{1}{2(L+\lambda)} & i &= 1, \ldots, 2L
\end{aligned} \tag{15}$$

$$\sum_{i=0}^{i=2L} \omega_i^{(c)} = 1, \quad \sum_{i=0}^{i=2L} \omega_i^{(m)} = 1 \tag{16}$$

where α and β are two tuned parameters for the filter. α affects the distribution of the sigma-points. The distribution of the sigma-points can affect the

convergence rate to some extent. And β controls the tails of the posterior distribution. In our experiments we set $\beta = 2$ and α varies from 0.1 to 2. Then compute the measured observation sigma points of each element of the sigma points matrix $\mathcal{X}_{k|k-1}$,

$$\mathcal{Y}_{k|k-1} = \mathbf{g}(\mathbf{x}_k, \mathcal{X}_{k|k-1}) \tag{17}$$

the prior of the mean of the measurements $\mathbf{d}_k^-$,

$$\hat{\mathbf{d}}_k^- = \sum_{i=0}^{2L} \omega_i^{(m)} \mathcal{Y}_{i,k|k-1} \tag{18}$$

the prior of the covariance matrix of the measurements $\mathbf{P}_{\mathbf{d}_k}^-$,

$$\mathbf{P}_{\mathbf{d}_k}^- = \sum_{i=0}^{2L} \omega_i^{(c)} (\mathcal{Y}_{i,k|k-1} - \hat{\mathbf{d}}_k^-)(\mathcal{Y}_{i,k|k-1} - \hat{\mathbf{d}}_k^-)^T + \mathbf{R}_{\mathbf{e}_k} \tag{19}$$

the cross covariance matrix for the parameter and the measurement,

$$\mathbf{P}_{\mathbf{w}_k \mathbf{d}_k} = \sum_{i=0}^{2L} \omega_i^{(c)} (\mathcal{X}_{i,k|k-1} - \hat{\mathbf{w}}_k^-)(\mathcal{Y}_{i,k|k-1} - \hat{\mathbf{d}}_k^-)^T \tag{20}$$

Compute the Kalman gain $\mathbf{K}_k$,

$$\mathbf{K}_k = \mathbf{P}_{\mathbf{w}_k \mathbf{d}_k} \mathbf{P}_{\mathbf{d}_k}^{-1} \tag{21}$$

Compute the posterior of the parameter and the posterior covariance of the parameter

$$\mathbf{w}_k = \mathbf{w}_k^- + \mathbf{K}_k(\mathbf{y}_n - \hat{\mathbf{d}}_k^-) \tag{22}$$

$$\mathbf{P}_{\mathbf{w}_k} = \mathbf{P}_{\mathbf{w}_k}^- - \mathbf{K}_k \mathbf{P}_{\mathbf{d}_k} \mathbf{K}_k^T \tag{23}$$

E. Coupled State Estimation

The hidden state variables for our dynamical system include the positions, the velocities, and the accelerations. Though the unscented Kalman Filter can be used for dual state-parameter estimation, the fact that the state and the parameters are coupled makes such a dual estimation fail to converge. Thus we use the finite difference method to estimate both the initial velocities and the accelerations. Given the observations of three frames $\mathbf{y}_{n-1}, \mathbf{y}_n, \mathbf{y}_{n+1}$ and the time elapsed between the frames Δt, the velocities $\dot{\mathbf{u}}$,

$$\dot{\mathbf{u}} = \frac{\mathbf{y}_n - \mathbf{y}_{n-1}}{\Delta t} \tag{24}$$

the accelerations $\ddot{\mathbf{u}}$,

$$\ddot{\mathbf{u}} = \frac{\mathbf{y}_{n+1} - 2\mathbf{y}_n + \mathbf{y}_{n-1}}{(\Delta t)^2} \tag{25}$$

Our dynamic parameter estimation scheme is given in Algorithm 1.

IV. RESULTS

We have implemented our algorithms in C/C++ and have validated the results by first conduct a synthetic heart experiment. In this experiment, we use 3D meshes from simulation as the deformation samples. We also validate our framework by reconstructing the Young's moduli of a tennis ball and of a foam ball from videos captured by high-speed cameras.

Algorithm 1 Dynamic Elasticity Parameter Estimation

1: **procedure** MEASUREMENT COMPUTATION
2:     // this is the function $\mathbf{g}$ in Eqn. 8.
3:     $\dot{\mathbf{u}} \leftarrow (\mathbf{y}_n - \mathbf{y}_{n-1})/\Delta t$
4:     $\ddot{\mathbf{u}} \leftarrow (\mathbf{y}_{n+1} - 2\mathbf{y}_n + \mathbf{y}_{n-1})/(\Delta t)^2$
5:     $\mathbf{d} \leftarrow \mathbf{f}(\mathbf{x};\mathbf{w})$ // evaluate measurement based on the parameters and the states
6: **end Measurement Computation**;
7: **procedure** UNSCENTED KALMAN FILTER ITERATE
8:     $\mathcal{X}_{k|k-1} \leftarrow [\hat{\mathbf{w}}_k^-, \hat{\mathbf{w}}_k^- + \gamma\sqrt{\mathbf{P}_{\mathbf{w}_k}^-}, \hat{\mathbf{w}}_k^- - \gamma\sqrt{\mathbf{P}_{\mathbf{w}_k}^-}]$
9:     // compute the sigma-points
10:     $\mathcal{Y}_{k|k-1} \leftarrow \mathbf{g}(\mathbf{x}_n, \mathbf{w}_k^-)$ // compute the prior of the mean of the measurement sigma-points
11:     $\hat{\mathbf{d}}_k^- \leftarrow \sum_{i=0}^{2L} \omega_i^{(m)} \mathcal{Y}_{i,k|k-1}$ // compute the prior of the covariance matrix of the measurement sigma-points
12:     $\mathbf{P}_{\mathbf{w}_k \mathbf{d}_k} \leftarrow \sum_{i=0}^{2L} \omega_i^{(c)} (\mathcal{X}_{i,k|k-1} - \hat{\mathbf{w}}_k^-)(\mathcal{Y}_{i,k|k-1} - \hat{\mathbf{d}}_k^-)^T$ // compute the cross covariance matrix of the measurements and the parameters
13:     $\mathbf{K}_k \leftarrow \mathbf{P}_{\mathbf{w}_k \mathbf{d}_k} \mathbf{P}_{\mathbf{d}_k}^{-1}$ // compute the Kalman gain
14:     $\hat{\mathbf{w}}_k \leftarrow \mathbf{w}_k^- + \mathbf{K}_k(\mathbf{y}_n - \hat{\mathbf{d}}_k^-)$
15:     // update the mean of the parameters
16:     $\mathbf{P}_{\mathbf{w}_k} \leftarrow \mathbf{P}_{\mathbf{w}_k}^- - \mathbf{K}_k \mathbf{P}_{\mathbf{d}_k} \mathbf{K}_k^T$
17:     // update the covariance matrix of the parameters
18: **end Unscented Kalman Filter Iterate**;
19: **procedure** MAIN
20:     **while** not converged **do**
21:         **for** Sampled Keyframes $\mathbf{y}_{n_i}$ **do**
22:             Initialize $\mathbf{x}_0, \mathbf{w}_0, \mathbf{P}_{\mathbf{w}_0}$
23:             Unscented Kalman Filter Iterate()
24:         **end for**;
25:     **end while**;
26: **end Main**;

Fig. 2. **The human heart anatomy.** In this project we model the left and right ventricle.© Texas Heart Institute [36]

the systole phase the volume of the heart reduced by around 40%. The computed heart contraction force with the model's Young's modulus being 40KPa is shown in Fig. 4. It ranges from 8.633mN to 37.40mN. This contraction force will serve as the boundary condition for solving the governing equation Eqn. 4. The observed deformation samples we feed into our framework are the 3D meshes from the synthetic simulation (shown in Fig. 5). We use deformation samples of two time stamp: a) the end of systole phase (shown in Fig. 5a) b) the end of diastole phase (shown in Fig. 5b).

The relative error for the recovered Young's modulus is within 7.5% of the ground-truth values, as shown in Table IV-A. The initial guess on the Young's modulus can contribute upto about 5% of relative error in the recovered value. We also measure the distance between the surface with optimized Young's modulus and the given reference surface using level set as another metric for validation. Our method can reduce the surface-tracking error down to less than 5%, as shown in Table IV-A, where the initial average separation distance between surfaces is 3.2mm. The average surface distance error between the tracked surface and the reference surface is shown in Table IV-A. These results show that our method can also be used to track the surfaces of the non-rigid bodies in the temporal sequences of deformation samples. The convergence graphs of the optimization process are shown in Fig. 6.

Possible Sources of Errors: 1) error introduced by the estimation of the velocities; 2) error introduced by incomplete information from the key frames; 3) error introduced by the sensitivity between the elasticity parameter and the amount of deformation.

B. Mechanical Parameters Recovered from Videos

We valid our framework further by recovering mechanical parameters of a tennis ball and a foam ball from videos captured by high-speed cameras. First, we reconstruct the 3D mesh from the video. We deduce 2D shape of the object from the video. Then we reconstruct the 3D shape by rotating the 2D shape (on the x,y plane) around the y-axis. Then we use our framework for estimation of non-rigid mechanical parameters. From the above synthetic experiment, we know the initialization can affect the accuracy of the method. We choose to initialize the Young's modulus after doing a line

A. Synthetic Heart Experiment

In this experiment, we recover the Young's modulus for a human heart from synthetic simulation results. We use 3D heart model reconstructed from a live patient ultrasound images, then simulate it with known Young's modulus and the computed contraction force using FEM. A human heart function by the contraction of the heart muscle of the right ventricle and right ventricle (shown in Fig. 2) to pump out blood. In this experiment, we will focus on the left and the right ventricles, because one of the main causes for diastolic dysfunction is due to the stiffening of muscles of the left or the right ventricle. We reconstructed our synthetic heart model from 3D ultrasound images [37] (shown in Fig. 3a-3b) using ITK-SNAP [38] to manually segment both the left and right ventricles (shown in Fig. 3c). We use Tetgen [39] to discretize the surface mesh for FEM simulation (shown in Fig. 3d). Then we use our statistical optimization framework to estimate both the Young's modulus and the state of the synthetic heart.

We compute the heart contraction force based on: a) the assumed Young's modulus; b) the statistics that by the end of
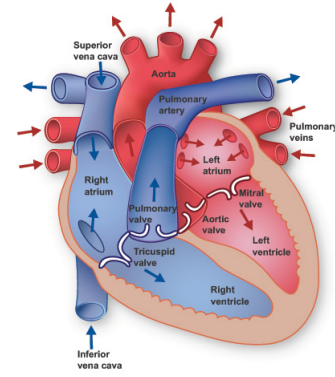
The result for the synthetic heart experiment with noises in the initialization. THE RELATIVE ERROR OF THE RECOVERED YOUNG'S MODULUS IS WITHIN 7.5% OF THE GROUND-TRUTH VALUES. OUR METHOD REDUCES THE AVERAGE SURFACE-TRACKING ERROR DOWN TO LESS THAN 5%.

Synthetic Young's Modulus (kPa)	40	80	100	140	180
Initialized Young's Modulus (kPa)	20±10	40±10	50±10	70±20	90±20
Recovered Young's Modulus (kPa)	37±2	76±3	93±4	134±7	167±10
Average Relative Error (%)	7.5	5	7	4.3	7.2
Standard Deviation of the Recovered Young's Modulus	1.41	2	3.2	7.5	10.2
Average Surface Distance Error (mm)	0.2±0.1	0.3±0.1	0.3±0.1	0.5±0.2	0.7±0.2
Average Relative Tracking Error (%)	1.3	2.0	2.0	3.3	4.7
Contraction Force Range (mN)	8-37	17-80	17-85	25-110	30-170
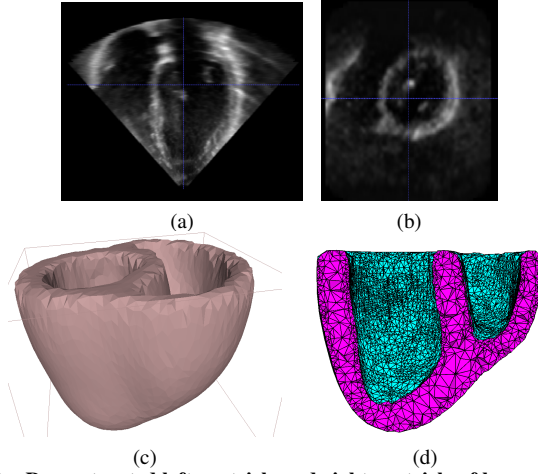
Fig. 3. **Reconstructed left ventricle and right ventricle of human heart.** (a)-(b) the slices of a human heart ultrasound image © CETUS 2014 [37], (c) the surface mesh of the reconstructed model, (d) the sliced view of the tetrahedra mesh from the surface mesh in (b).
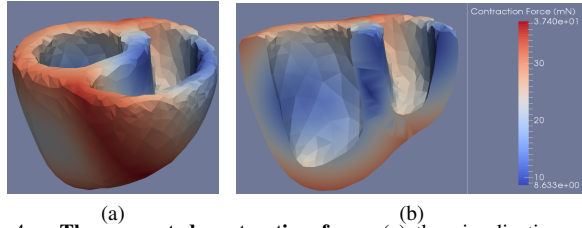
Fig. 4. **The computed contraction force.** (a) the visualization of the contraction force on the surface of the 3D heart model using cool to hot color map, (b) the sliced view of the contraction force.
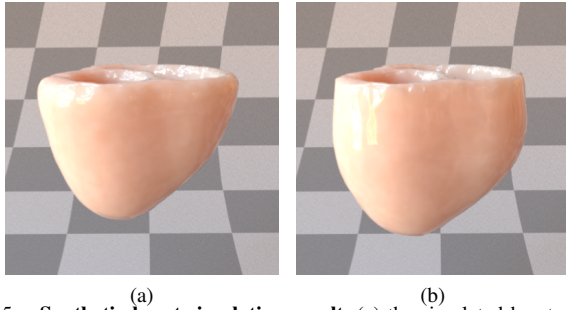

Fig. 5. **Synthetic heart simulation result.** (a) the simulated heart model by the end of systole phase, (b) the simulated heart model by the end of diastole phase.
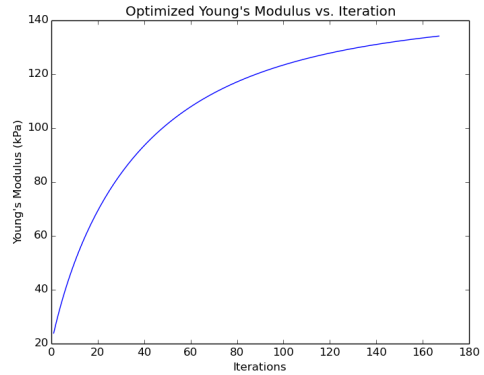
search. This process can greatly reduce the optimization iterations and increase the speed as well.

The boundary condition for both the videos are the gravity. The average density of a tennis ball is $0.4g/cm^3$ and that of a foam ball is around $30g/cm^3$.

From the tennis ball video (clips shown in 7a- 7e), we recovered the Young's modulus to be 2.2-2.5MPa. The
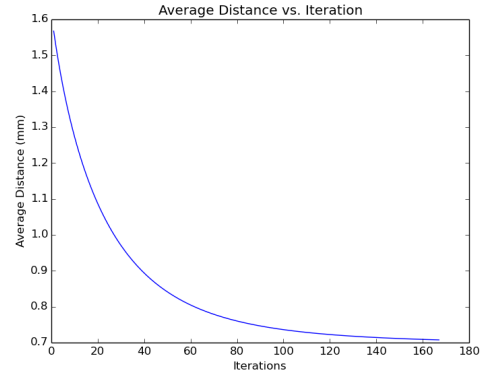
Fig. 6. **The convergence graphs for synthetic heart experiment.** (a) shows our framework reduces the distance between the surface with the optimized material parameter and the reference surface, as the framework iterates with the initial distance error at 3.2mm, (b) shows the convergence of the Young's modulus to the ground truth.

surface meshes of the model with optimized mechanical parameters and states are shown in 7f- 7j. The Young's modulus we recovered is within the range of the values measured in the work [40], [41]. The estimated velocities of the tennis ball (before it hit the flat surface) from the video is about 20m/s. For the foam ball, the Young's modulus we recovered is about 15-21KPa. According to the video description, the foam ball in the video (clips shown in 8a-8e) is a stress relief foam ball. This type of foam ball is made of polyurethane foam. Our estimated parameter is well within the range presented in the literature [42]. One of the sources of error is the estimated initial value to the state estimation. Currently we estimated the initial velocity with a finite difference technique using the first couple video frames. We conducted a study using the tennis ball data with
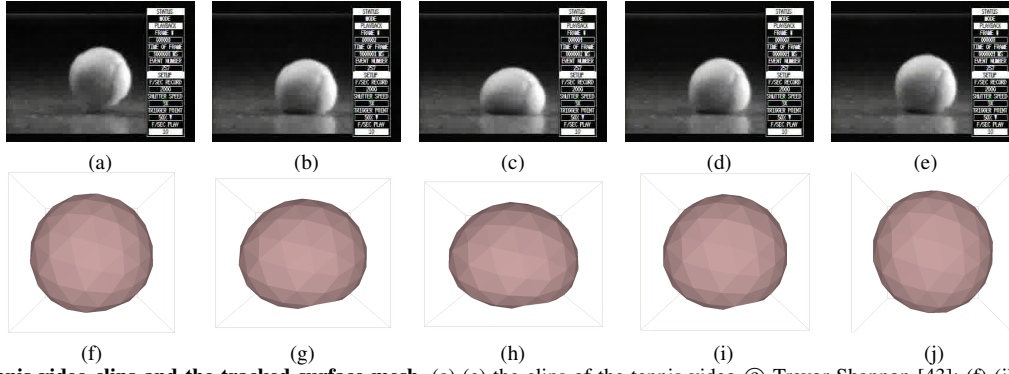
Fig. 7. **Input tennis video clips and the tracked surface mesh.** (a)-(e) the clips of the tennis video © Trevor Shannon [43]; (f)-(j) the tracked surface mesh at the corresponding time stamp.
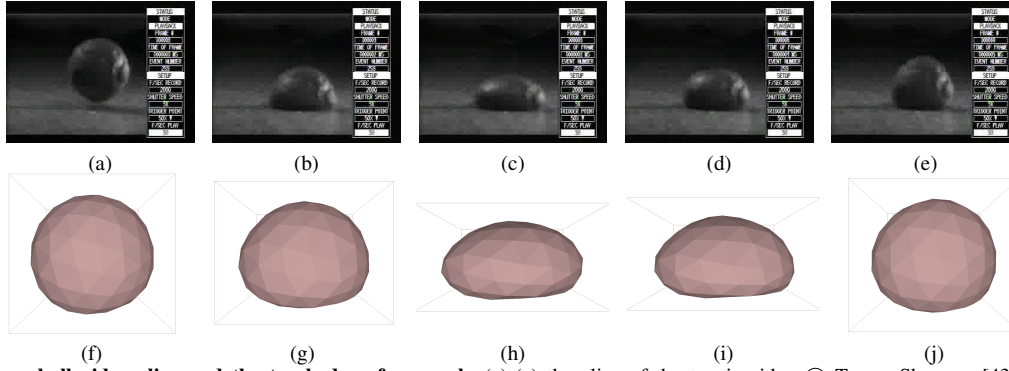

Fig. 8. **Input foam ball video clips and the tracked surface mesh.** (a)-(e) the clips of the tennis video © Trevor Shannon [43]; (f)-(j) the tracked surface mesh at the corresponding time stamp.

different velocity magnitude before hitting the surface. The initial velocities could affect the recovered Young's modulus shown in Table IV-B. One reason for how much it affects the recovered Young's modulus is the size of the object. The impact of initial-value estimation is reduced as the size of the object increases.

We also compare our method with the most recent work by Wang et al. [30]. They also use temporal sequences of deformation samples as input, but they assume the deformable objects are in static state. As is shown in Table IV-B, our results are much closer to the measured parameters from real-world experiments. Please see the supplementary video for demonstration of these experiments.

TABLE II

Impact of initial velocities on recovered Young's moduli.

Initial Vel Mag (m/s)	0	0.01	20
Recovered E (kPa)	5.1-5.9	$6.2e^2$-$6.9e^2$	$2.2e^3$-$2.5e^3$

TABLE III

Comparison with results of [30] and experimental measurements.

THE MEASURED YOUNG'S MODULUS FOR THE TENNIS BALL IS TAKEN FROM [40], [41] AND FOR THE FOAM BALL IS DERIVED FROM [42]. THE RECOVERED YOUNG'S MODULUS USING OUR METHOD IS WITHIN THE RANGE OF THE YOUNG'S MODULUS MEASURED, THE YOUNG'S MODULUS RECOVERED USING [30] IS NOT.

	Tennis Ball	Foam Ball
Wang et al. [30] E (KPa)	5.1-5.9	0.1-0.2
Our method E (KPa)	$2.2e^3$-$2.5e^3$	12-21
Measured E (KPa)	$1e^3$-$5e^3$	10-30

V. DISCUSSION AND CONCLUSION

In this paper, we presented a Bayesian parameter estimation framework for dynamic deformable bodies. Our inputs are temporal sequences of deformation samples, such as simulation results or videos from ultrasound and high-speed cameras. This approach uses the Unscented Kalman Filter for hidden parameter estimation to recover the Young's modulus, tightly coupled with a simulation-based state estimation for surface tracking/matching. The results from synthetic experiments and validation using real-life videos demonstrate the effectiveness of the proposed method in estimating the mechanical properties of the deformable bodies in motion.

For nonrigid bodies, state estimation still remains a challenging problem. The boundary conditions in our framework are known or can be computed. In many real-life situations, the boundary conditions can be complicated to derive. Detailed analysis and study on the impact of the boundary conditions would be possible avenues for future research, when applying this framework to different problem domains.

ACKNOWLEDGMENT

REFERENCES

[1] D. Veronda and R. Westmann, "Mechanical characterization of skin-finite deformations," *Journal of biomechanics*, vol. 3, no. 1, pp. 111–124, 1970.

[2] J. Ophir, I. Cespedes, H. Ponnekanti, Y. Yazdi, and X. Li, "Elastography: a quantitative method for imaging the elasticity of biological tissues," *Ultrasonic imaging*, vol. 13, no. 2, pp. 111–134, 1991.

[3] M. Kauer, V. Vuskovic, J. Dual, G. Székely, and M. Bajka, "Inverse finite element characterization of soft tissues," *Medical Image Analysis*, vol. 6, no. 3, pp. 275–287, 2002.

[4] H.-P. Lee, M. Foskey, M. Niethammer, P. Krajcevski, and M. C. Lin, "Simulation-Based Joint Estimation of Body Deformation and Elasticity Parameters for Medical Image Analysis," *Medical Imaging, IEEE Transactions on*, vol. 31, no. 11, pp. 2156 –2168, nov. 2012.

[5] J. J. Moré, "The levenberg-marquardt algorithm: implementation and theory," in *Numerical analysis*. Springer, 1978, pp. 105–116.

[6] M. Lourakis and A. Argyros, "The design and implementation of a generic sparse bundle adjustment software package based on the levenberg-marquardt algorithm," Technical Report 340, Institute of Computer Science-FORTH, Heraklion, Crete, Greece, Tech. Rep., 2004.

[7] K. Loague and R. E. Green, "Statistical and graphical methods for evaluating solute transport models: overview and application," *Journal of contaminant hydrology*, vol. 7, no. 1, pp. 51–73, 1991.

[8] D. Madigan, J. York, and D. Allard, "Bayesian graphical models for discrete data," *International Statistical Review/Revue Internationale de Statistique*, pp. 215–232, 1995.

[9] E. Wan, R. Van Der Merwe, *et al.*, "The unscented kalman filter for nonlinear estimation," in *Adaptive Systems for Signal Processing, Communications, and Control Symposium 2000. AS-SPCC. The IEEE 2000*. IEEE, 2000, pp. 153–158.

[10] H. Mehrabian and A. Samani, "Constrained hyperelastic parameters reconstruction of pva (polyvinyl alcohol) phantom undergoing large deformation," in *SPIE Medical Imaging*. International Society for Optics and Photonics, 2009, pp. 72 612G–72 612G.

[11] M. P. Ottensmeyer, "Minimally invasive instrument for in vivo measurement of solid organ mechanical impedance," Ph.D. dissertation, Massachusetts Institute of Technology, 2001.

[12] I. Brouwer, J. Ustin, L. Bentiey, A. Dhruv, and F. Tendick, "Measuring in vivo animal soft tissue properties for haptic modeling in surgical," in *Medicine meets virtual reality*, vol. 81, 2001, p. 69.

[13] P. Boonvisut and M. C. Cavusoglu, "Estimation of soft tissue mechanical parameters from robotic manipulation data," *Mechatronics, IEEE/ASME Transactions on*, vol. 18, no. 5, pp. 1602–1611, 2013.

[14] J. Rogowska, N. Patel, S. Plummer, and M. Brezinski, "Quantitative optical coherence tomographic elastography: method for assessing arterial mechanical properties," *The British journal of radiology*, 2014.

[15] A. J. Engel and G. R. Bashford, "Enabling real-time ultrasound imaging of soft tissue mechanical properties by simplification of the shear wave motion equation," in *Engineering in Medicine and Biology Society (EMBC), 2015 37th Annual International Conference of the IEEE*. IEEE, 2015, pp. 3831–3834.

[16] L. E. Bilston and K. Tan, "Measurement of passive skeletal muscle mechanical properties in vivo: recent progress, clinical applications, and remaining challenges," *Annals of biomedical engineering*, vol. 43, no. 2, pp. 261–273, 2015.

[17] E. L. Howes, J. W. Sooy, and S. C. Harvey, "The healing of wounds as determined by their tensile strength," *Journal of the American Medical Association*, vol. 92, no. 1, pp. 42–45, 1929.

[18] A. Glaser, R. Marangoni, J. Must, T. Beckwith, G. Brody, G. Walker, and W. White, "Refinements in the methods for the measurement of the mechanical properties of unwounded and wounded skin," *Medical electronics and biological engineering*, vol. 3, no. 4, pp. 411–419, 1965.

[19] P. Pathmanathan, D. J. Gavaghan, J. P. Whiteley, S. J. Chapman, and J. M. Brady, "Predicting tumor location by modeling the deformation of the breast," *Biomedical Engineering, IEEE Transactions on*, vol. 55, no. 10, pp. 2471–2480, 2008.

[20] F. S. Azar, D. N. Metaxas, and M. D. Schnall, "Methods for modeling and predicting mechanical deformations of the breast under external perturbations," *Medical Image Analysis*, vol. 6, no. 1, pp. 1–27, 2002.

[21] M. P. Ottensmeyer and J. K. Salisbury Jr, "In vivo data acquisition instrument for solid organ mechanical property measurement," in *Medical Image Computing and Computer-Assisted Intervention–MICCAI 2001*. Springer, 2001, pp. 975–982.

[22] I. Sakuma, Y. Nishimura, C. K. Chui, E. Kobayashi, H. Inada, X. Chen, and T. Hisada, "In vitro measurement of mechanical properties of liver tissue under compression and elongation using a new test piece holding method with surgical glue," in *Surgery Simulation and Soft Tissue Modeling*. Springer, 2003, pp. 284–292.

[23] S. Es' haghian, P. Gong, K. M. Kennedy, P. Wijesinghe, D. D. Sampson, R. A. McLaughlin, and B. F. Kennedy, "In vivo optical elastography: stress and strain imaging of human skin lesions," in *SPIE BiOS*. International Society for Optics and Photonics, 2015, pp. 93 270C–93 270C.

[24] Z. Han, J. Li, M. Singh, C. Wu, C.-h. Liu, S. Wang, R. Idugboe, R. Raghunathan, N. Sudheendran, S. R. Aglyamov, *et al.*, "Quantitative methods for reconstructing tissue biomechanical properties in optical coherence elastography: a comparison study," *Physics in medicine and biology*, vol. 60, no. 9, p. 3531, 2015.

[25] D. H. Cortes, S. M. Suydam, K. G. Silbernagel, T. S. Buchanan, and D. M. Elliott, "Continuous shear wave elastography: A new method to measure viscoelastic properties of tendons in vivo," *Ultrasound in medicine & biology*, vol. 41, no. 6, pp. 1518–1529, 2015.

[26] R. Chopra, A. Arani, Y. Huang, M. Musquera, J. Wachsmuth, M. Bronskill, and D. Plewes, "In vivo MR elastography of the prostate gland using a transurethral actuator," *Magnetic Resonance in Medicine*, vol. 62, no. 3, pp. 665–671, Sept. 2009. [Online]. Available: http://dx.doi.org/10.1002/mrm.22038

[27] C. Syllebranque, S. Boivin, C. Duriez, and C. Chaillou, "Estimation of hookean parameters of deformable bodies from real videos," in *Cyberworlds, 2007. CW'07. International Conference on*. IEEE, 2007, pp. 330–337.

[28] B. Bickel, M. Bächer, M. A. Otaduy, H. R. Lee, H. Pfister, M. Gross, and W. Matusik, "Design and fabrication of materials with desired deformation behavior," *ACM Transactions on Graphics (TOG)*, vol. 29, no. 4, p. 63, 2010.

[29] H. Xu, Y. Li, Y. Chen, and J. Barbivč, "Interactive material design using model reduction," *ACM Transactions on Graphics (TOG)*, vol. 34, no. 2, p. 18, 2015.

[30] B. Wang, L. Wu, K. Yin, U. Ascher, L. Liu, and H. Huang, "Deformation capture and modeling of soft objects," *ACM Transactions on Graphics (TOG)*, vol. 34, no. 4, p. 94, 2015.

[31] E. J. Lefferts, F. L. Markley, and M. D. Shuster, "Kalman filtering for spacecraft attitude estimation," *Journal of Guidance, Control, and Dynamics*, vol. 5, no. 5, pp. 417–429, 1982.

[32] R. Zhan and J. Wan, "Iterated unscented kalman filter for passive target tracking," *Aerospace and Electronic Systems, IEEE Transactions on*, vol. 43, no. 3, pp. 1155–1163, 2007.

[33] M. H. Moghari and P. Abolmaesumi, "Point-based rigid-body registration using an unscented kalman filter," *Medical Imaging, IEEE Transactions on*, vol. 26, no. 12, pp. 1708–1728, 2007.

[34] S. Tak and H.-S. Ko, "A physically-based motion retargeting filter," *ACM Transactions on Graphics (TOG)*, vol. 24, no. 1, pp. 98–117, 2005.

[35] S. Dambreville, Y. Rathi, and A. Tannenbaum, "Tracking deformable objects with unscented kalman filtering and geometric active contours," in *American Control Conference, 2006*. IEEE, 2006, pp. 6–pp.

[36] T. H. Institute, http://www.texasheart.org/HIC/Anatomy/anatomy2.cfm, 1996.

[37] O. Bernard, B. Heyde, M. Alessandrini, D. Barbosa, S. Camarasu-Pop, F. Cervenansky, S. Valette, O. Mirea, E. Galli, M. Geleijnse, *et al.*, "Challenge on endo-cardial three-dimensional ultrasound segmentation (cetus)," *Proceedings of the MICCAI Challenge on Endocardial Three-dimensional Ultrasound Segmentation-CETUS*, pp. 1–8, 2014.

[38] P. A. Yushkevich, J. Piven, H. Cody Hazlett, R. Gimpel Smith, S. Ho, J. C. Gee, and G. Gerig, "User-guided 3D active contour segmentation of anatomical structures: Significantly improved efficiency and reliability," *Neuroimage*, vol. 31, no. 3, pp. 1116–1128, 2006.

[39] H. Si, "Tetgen, a delaunay-based quality tetrahedral mesh generator," *ACM Trans. Math. Softw.*, vol. 41, no. 2, pp. 11:1–11:36, Feb. 2015. [Online]. Available: http://doi.acm.org/10.1145/2629697

[40] L. Sissler, R. Jones, P. Leaney, and A. Harland, "Viscoelastic modelling of tennis ball properties," in *IOP Conference Series: Materials Science and Engineering*, vol. 10, no. 1. IOP Publishing, 2010, p. 012114.

[41] K. Wójcicki, K. Puciłowski, and Z. Kulesza, "Mathematical analysis for a new tennis ball launcher," *acta mechanica et automatica*, vol. 5, pp. 110–119, 2011.

[42] B. Moore, T. Jaglinski, D. Stone, and R. Lakes, "On the bulk modulus of open cell foams," *Cellular Polymers*, vol. 26, no. 1, pp. 1–10, 2007.

[43] T. Shannon, http://www.trevorshp.com/photography/hsi_videos/index.htm, 2009.